

Electronic Supplementary Material (ESI) for Energy & Environmental Science.

This journal is © The Royal Society of Chemistry 2020

Supplementary Information for

Scalable Surface Engineering of Commercial Metal Foams for Defect-rich Hydroxides towards Improved Oxygen Evolution

Guoxing Zhu,^{*ad} Xiaoyun Li,^a Yuanjun Liu,^b Yu Mao,^{*c} Zhiwu Liang,^c Zhenyuan Ji,^a
Xiaoping Shen,^a Jian Sun,^d Xiaofang Cheng,^b and Junjie Mao^{*d}

^aSchool of Chemistry and Chemical Engineering, Jiangsu University, Zhenjiang
212013, China, E-mail: zhuguoxing@ujs.edu.cn

^bSchool of Environmental and Chemical Engineering, Jiangsu University of Science
and Technology, Zhenjiang 202018, China

^cCollege of Chemistry and Chemical Engineering, Hunan University, Changsha,
410082, China, E-mail: yumao@outlook.com

^dCollege of Chemistry and Materials Science, Anhui Normal University, Wuhu,
241000, China, E-mail: maochem@ahnu.edu.cn

S1. X-ray absorption fine structure spectra (XAFS) measurements

XAFS measurements were conducted on BL1W1B station (Beijing Synchrotron Radiation Facility, China). The data was collected in fluorescence excitation mode. The ATHENA module was used to process the acquired extended XAFS (EXAFS) data. k^3 -Weighted $\chi(k)$ data of Fe K-edge were Fourier transformed to real (R) space using a hanning windows ($dk=1.0 \text{ \AA}^{-1}$) to separate the EXAFS contributions from different coordination shells.

To obtain the quantitative structural parameters around central atoms, least-squares curve parameter fitting was performed using the ARTEMIS module of IFEFFIT software packages.

The following EXAFS equation was used:

$$\chi(k) = \sum_j \frac{N_j S_0^2 F_j(k)}{k R_j^2} \exp[-2k^2 \sigma_j^2] \exp\left[-\frac{2R_j}{\lambda(k)}\right] \sin[2k R_j + \phi_j(k)]$$

N_j is the number of neighbors in the j^{th} atomic shell, S_0^2 is the amplitude reduction factor, $F_j(k)$ is the effective curved-wave backscattering amplitude, R_j is the distance between the X-ray absorbing central atom and the atoms in the j^{th} atomic shell (back scatterer), λ is the mean free path in \AA , $\phi_j(k)$ is the phase shift (including the phase shift for each shell and the total central atom phase shift), σ_j is the Debye-Waller parameter of the j^{th} atomic shell (variation of distances around the average R_j). The functions $F_j(k)$, λ and $\phi_j(k)$ were calculated with the ab initio code FEFF8.2.

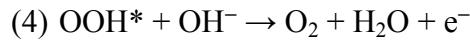
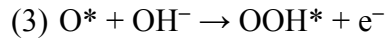
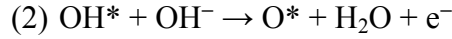
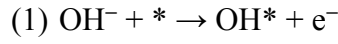
S2. Details of the first-principles Density functional theory calculations

The calculations were performed with the Perdew-Burke-Ernzerh (PBE) functional using Vienna ab initio simulation package (VASP) with the project-augmented wave (PAW) method used to represent the core-valence interaction.¹⁻⁵ For the calculations of total energy, 450 eV of cut-off energy was set for plane wave basis set to expand the valence electronic states. D3 correction was used to include van der Waals (vdW) interactions.⁶ Spin polarization was also considered. The effective U-J values were set as 3.50 and 3.53 eV for Fe and Co, respectively.⁷⁻⁹ The Brillouin zone was sampled at

Γ point; and a vacuum layer of 15 Å was used. The atoms were fully relaxed until the force on them <0.05 eV/Å. Bader analysis was also conducted.¹⁰

The structure model of layered CoFe-hydroxides with or without oxygen vacancies were first optimized. The surface model, two pristine Co(OH)₂ layers with spacing of 2.72 Å ((101) plane of CoFe layered double metal hydroxides⁹), was constructed (4×4 supercell) (shown in Figure 4a in the main text).¹¹⁻¹² The half atoms of the upper layer were then removed to expose the reaction sites. Then, half of Co atoms are replaced by Fe atoms to satisfy the experimental ratio of about 1:1. Two adjacent hydrogen ions were removed from the upper layer to mimic the influence of interlayer CO₃²⁻ and H₂O molecular, thus CoFeOH was oxidized to CoFeOOH (CoFe LDHs). It should be noted that there are two different structures after removing the two H atoms, the more stable one is chosen for this study.

In our case, the OER is operated in 1 M KOH, the elementary steps can be written as follows.^{7, 13}



The Gibbs free energy change for steps 1-4 can be expressed as:

$$\Delta G_1 = \Delta G_{\text{OH}} - eU + \Delta G_{\text{H}^+}(\text{pH})$$

$$\Delta G_2 = \Delta G_{\text{O}} - \Delta G_{\text{OH}} - eU + \Delta G_{\text{H}^+}(\text{pH})$$

$$\Delta G_3 = \Delta G_{\text{OOH}} - \Delta G_{\text{O}} - eU + \Delta G_{\text{H}^+}(\text{pH})$$

$$\Delta G_4 = 4.92 - \Delta G_{\text{OOH}} - eU + \Delta G_{\text{H}^+}(\text{pH})$$

Where U is the potential measured against normal hydrogen electrode (NHE) at standard conditions. The free energy change of the protons relative to the above specified electrode at non-zero pH (in our cases, pH = 13.6) is represented by Nernst equation as:

$$\Delta G_{\text{H}^+}(\text{pH}) = -k_B T \ln(10) * \text{pH}$$

The sum of ΔG_{1-4} is fixed to the negative of experimental Gibbs free energy of formation of two water molecules ($1.23 * 4 = 4.92$ eV) to avoid the calculation of the O_2 bond energy, which is difficult to accurately determine within current computational setting. The Gibbs free energy differences of these intermediates include zero-point energy (ZPE), thermal energy and entropy derived from partition functions.¹⁴⁻¹⁵ The ZPE correction is given by:

$$E_{ZPE} = \sum_i \frac{h\nu_i}{2}$$

where h is Plank's constant and ν_i is vibrational frequency that is calculated based on the harmonic oscillator approximation. The standard molar vibrational thermal energy contribution is calculated by:

$$U_{vib} = RT \sum_i \frac{h\nu_i/k_B}{e^{h\nu_i/k_B T} - 1}$$

where R is the gas constant and k_B is Boltzmann's constant. The standard molar vibrational entropy is calculated using the following expression:

$$S_{vib} = R \sum_i \left[\frac{h\nu_i/k_B T}{e^{h\nu_i/k_B T} - 1} - \ln(1 - e^{-h\nu_i/k_B T}) \right]$$

Therefore, the standard molar Gibbs free energies are obtained by:

$$G = E_{total} + E_{ZPE} + U - TS$$

$$\Delta G = \Delta E_{total} + \Delta(E_{ZPE} + U - TS)$$

where E_{total} refers to the total energy obtained from DFT calculation. The energy difference ΔE is calculated relative to H_2O and O_2 :

$$\Delta E_{OH} = E_{OH} - E_{Surface} - (E_{H_2O} - 1/2 E_{H_2})$$

$$\Delta E_O = E_O - E_{Surface} - (E_{H_2O} - E_{H_2})$$

$$\Delta E_{OOH} = E_{OOH} - E_{Surface} - (2 * E_{H_2O} - 3/2 E_{H_2})$$

After obtaining all ΔG via above equations, the theoretical overpotential is then readily defined as the maximum of ΔG_1 , ΔG_2 , ΔG_3 , ΔG_4 (divided by e) that minus 1.23 V.

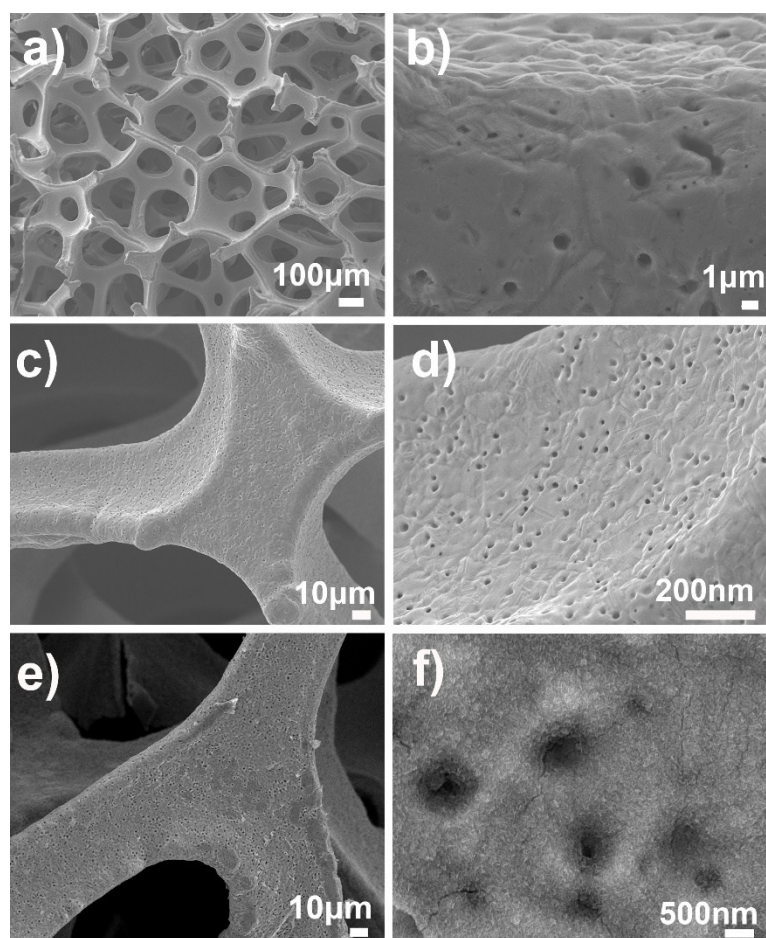


Fig. S1 SEM images of a, b) the original Co foam, c, d) the cleaned Co foam, and e, f) the obtained Co/Fe³⁺ foam.

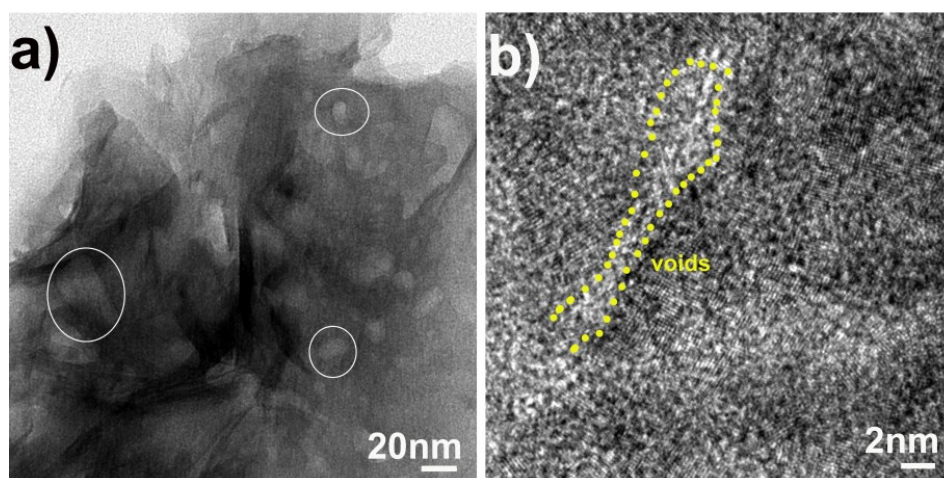


Fig. S2 TEM images of the sample scraped from Co/Fe³⁺ product showing a) porous structure and b) tiny voids on the nanosheets.

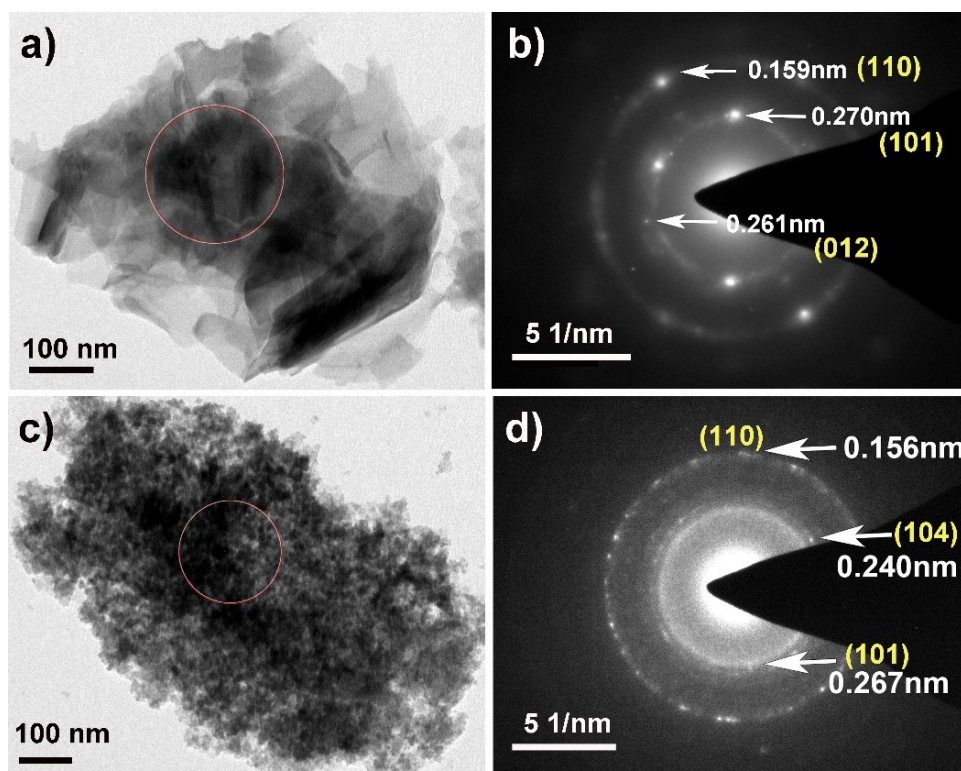


Fig. S3 TEM images and the corresponding SAED analyses. a, b) Co/Fe³⁺ and c, d) Ni/Fe³⁺.

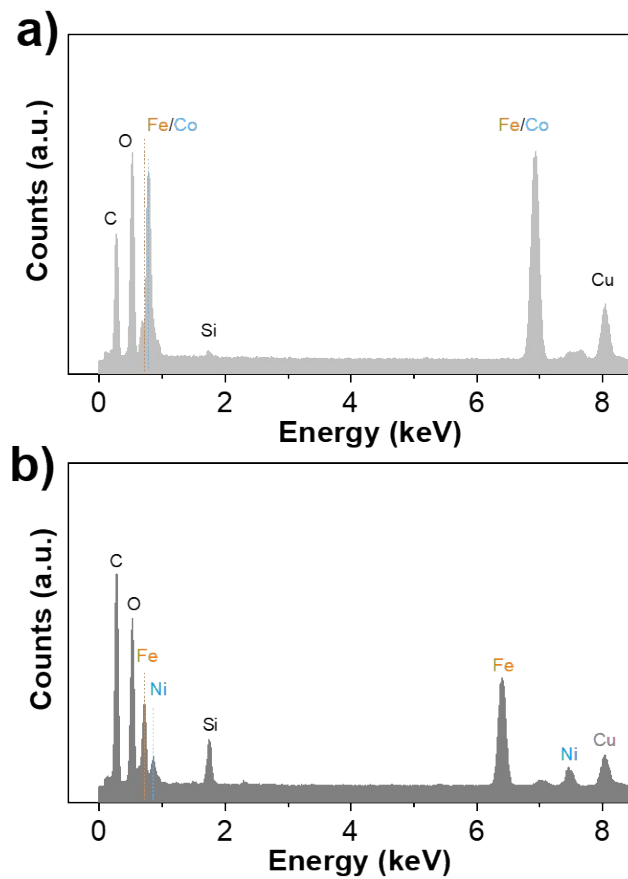


Fig. S4 EDS analyses for a) Co/Fe³⁺ and b) Ni/Fe³⁺ products. The signals of Fe and Co are partially overlapped. In the spectra, the presence of Si element is caused by the detector used for the collection of EDS. The presence of Cu comes from the carbon coated copper grid used to load the samples for TEM observation and EDS analyses; the signal of C is partially from the carbon coated copper grid.

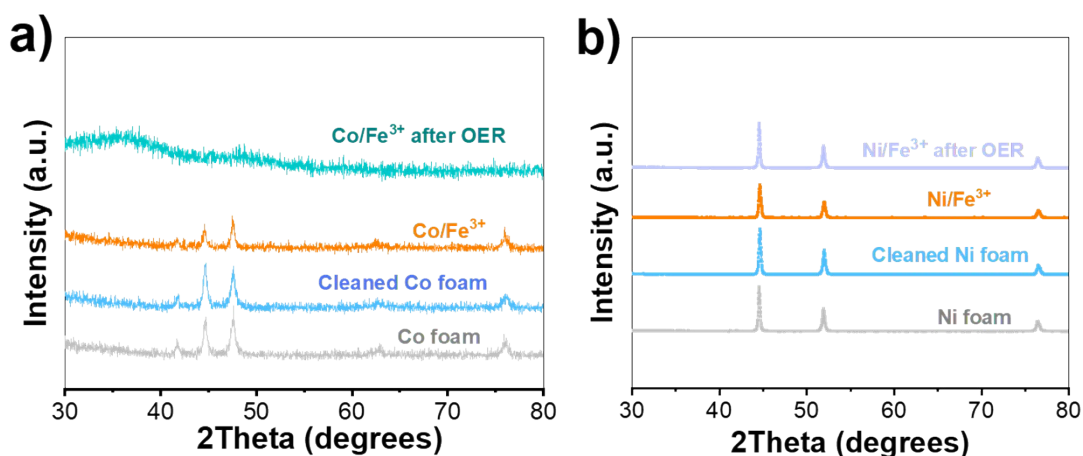


Fig. S5 XRD patterns of a) the original cobalt foam, cleaned Co foam, Co/Fe³⁺ foam, and Co/Fe³⁺ product after OER, b) the original nickel foam, cleaned Ni foam, Ni/Fe³⁺ foam, and Ni/Fe³⁺ product after OER.

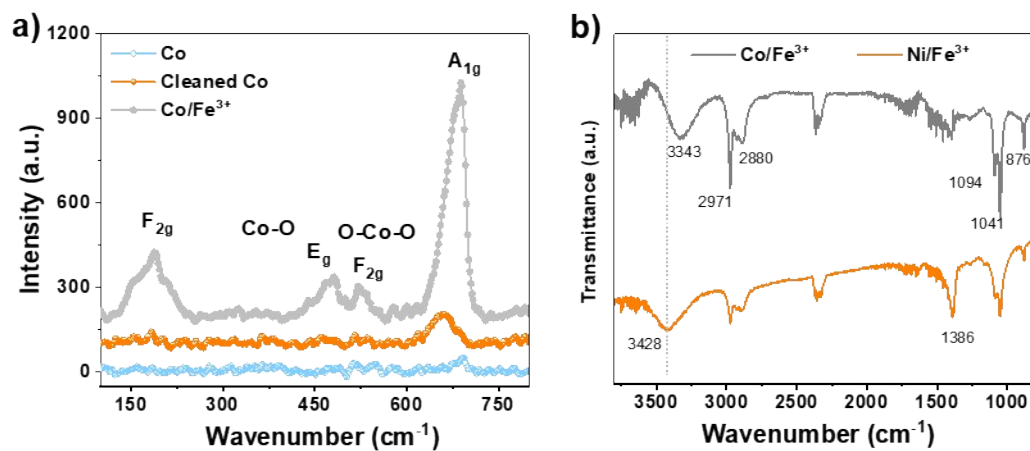


Fig. S6 a) Raman spectra of the Co foam, cleaned Co, and Co/Fe³⁺ products. b) FT-IR spectra of the surface layer scraped from Co/Fe³⁺ and Ni/Fe³⁺ product surface.

The two products Ni/Fe³⁺ and Co/Fe³⁺ show quite similar IR spectra, although the Co/Fe³⁺ foam has a relatively stronger background. The two products only show different stretching vibrations of O-H unit that presents a wide band at 3428 cm⁻¹ for Ni/Fe³⁺ and at 3343 cm⁻¹ for Co/Fe³⁺ product. The slight difference of this band would be caused by the different degree of hydrogen-bonding in the samples.

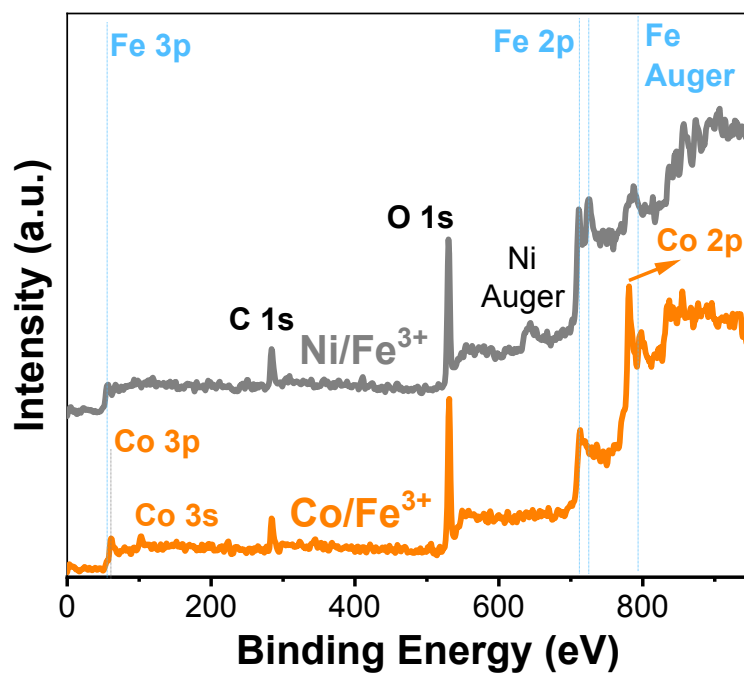


Fig. S7 XPS survey spectra for Ni/Fe³⁺ and Co/Fe³⁺ products.

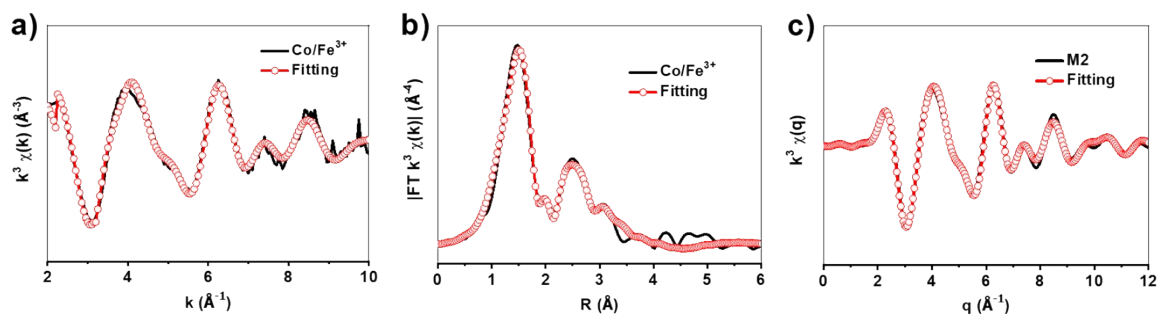


Fig. S8 EXAFS fitting curves of Co/Fe³⁺ foam at (a) k space, (b) R and (c) q space.

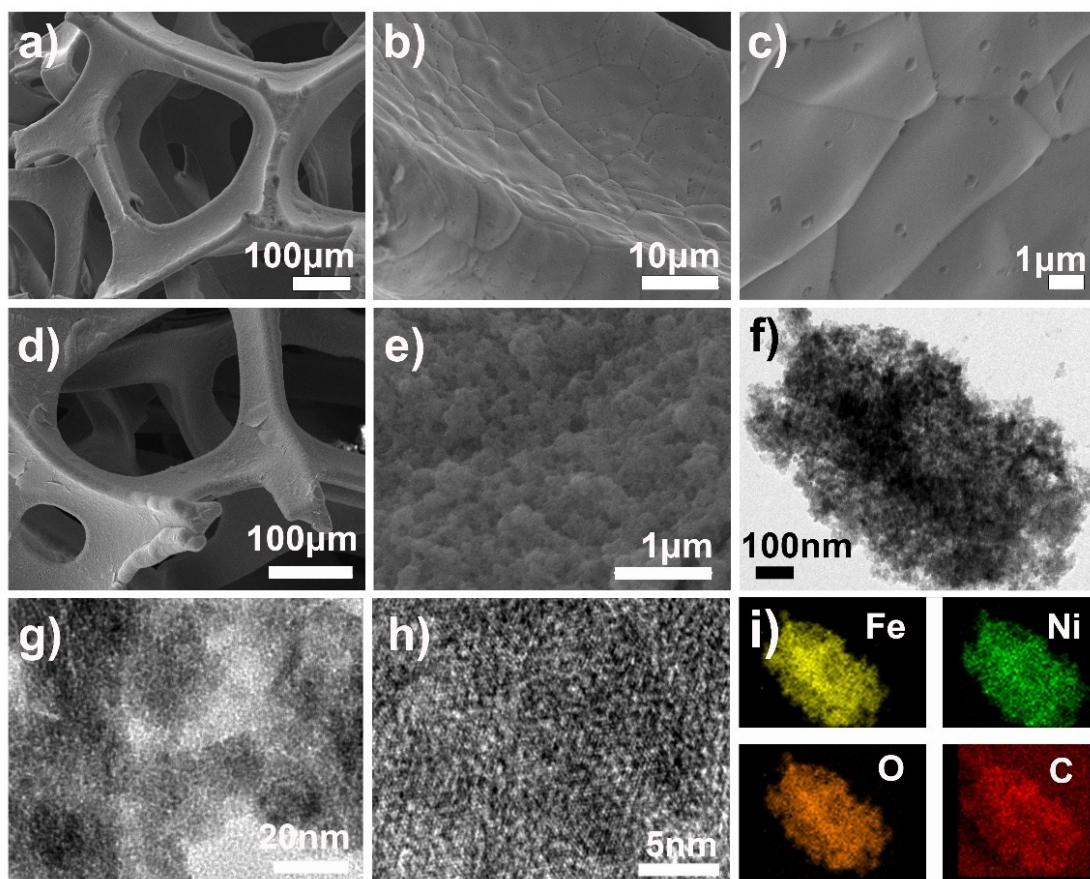


Fig. S9 SEM images of a-c) the cleaned Ni foam and d, e) the prepared Ni/Fe³⁺ product; f-h) TEM and HRTEM images of the product scarpred from Ni/Fe³⁺ surface; i) Element mapping analysis of the product on Ni/Fe³⁺ surface with region of f).

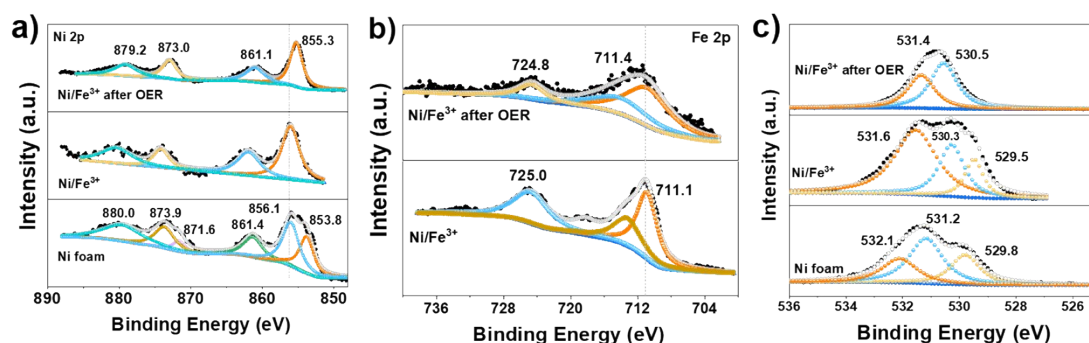


Fig. S10 XPS spectra of the cleaned Ni foam, Ni/Fe³⁺ product, and Ni/Fe³⁺ electrode after OER operation; a) Ni 2p, b) Fe 2p and b) O 1s.

The Ni 2p spectrum of bare Ni foam presents peaks at 853.8 and 871.6 eV corresponding to Ni 2p_{3/2} and Ni 2p_{1/2}, respectively, suggesting the presence of metallic Ni (Fig. S10a). Another two bands at 856.1 and 873.9 eV indicate the presence of Ni(II) species that is due to the surface oxidation of metal foam in air. The two shakeup satellites locate at 861.4 and 880.0 eV. With the Fe³⁺ treatment process, the formed Ni/Fe³⁺ product only shows the bands of Ni(II), suggesting the oxidation of surface metallic Ni during the Fe³⁺ treatment process (Fig. S10a). Similar to that of Co/Fe³⁺ product, XPS band of Fe 2p in the Ni/Fe³⁺ product shows the presence of Fe(III) species (Fig. S10b). XPS spectra of O 1s for Ni foam and Ni/Fe³⁺ products are basically consistent with those of Co-based products (Fig. S10c).

After OER operation, the XPS band of Ni 2p_{3/2} red-shifts to 855.3 eV, indicating the chemical environment change of Ni sites. The XPS band of Fe did not present obvious change after OER. As for oxygen element, the main band locates at 530.5 eV that corresponds to M-OH. This confirms the formation of metal hydroxides during electrolytic process. This is different from that of Co/Fe³⁺, in that case, CoOOH was formed.

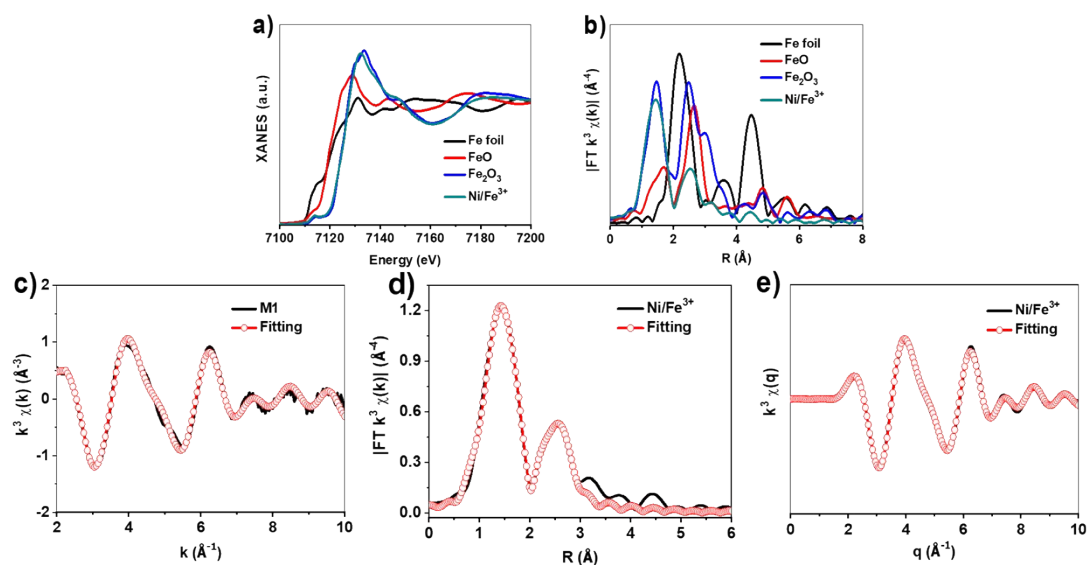


Fig. S11 a) XANES spectra, b) Fourier transform (FT) of the Fe K-edge of Ni/Fe³⁺ foam, FeO, Fe₂O₃, and Fe foil. EXAFS fitting curves of Ni/Fe³⁺ foam at (c) k space, (d) R and (e) q space.

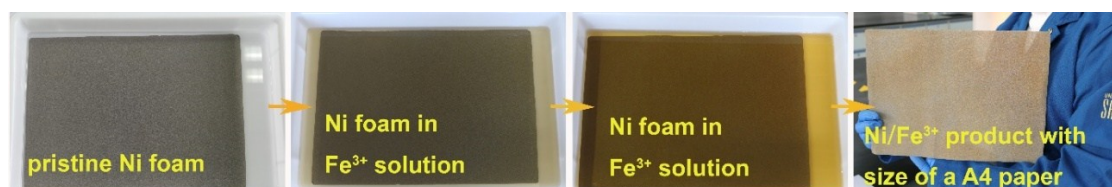


Fig. S12 Digital images showing the scaled-up preparation of Ni/Fe³⁺ product with size of a A4 paper.

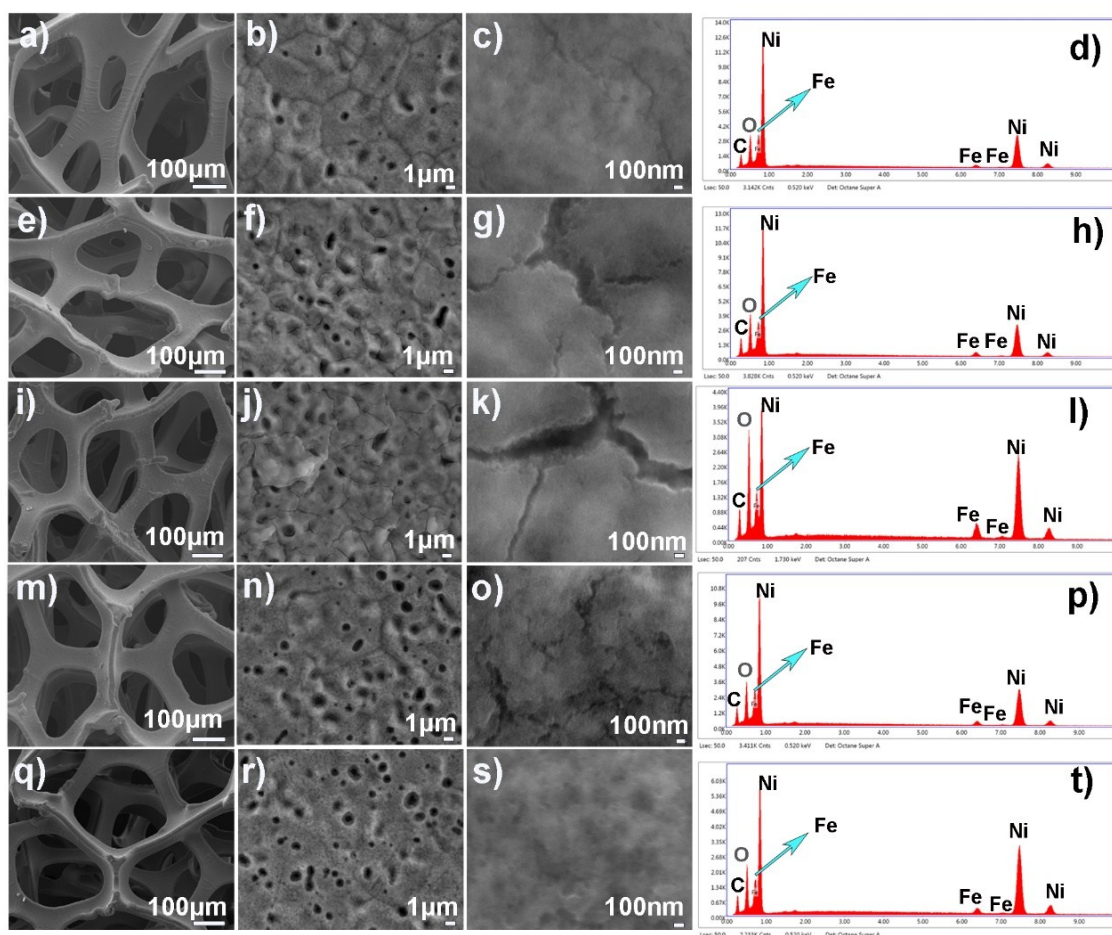


Fig. S13 SEM images and EDS spectra for five randomly selected small pieces from scaled-up preparation of Ni/Fe³⁺ product shown in the above digital image. a-d) piece of No. 1, showing Fe:Ni ratio of 0.063:1, e-h) piece No. 2 showing Fe:Ni ratio of 0.040:1, i-l) piece of No. 3 showing Fe:Ni ratio of 0.073:1, m-p) piece of No. 4 showing Fe:Ni ratio of 0.046:1, q-t) piece of No. 5 showing Fe:Ni ratio of 0.040:1.

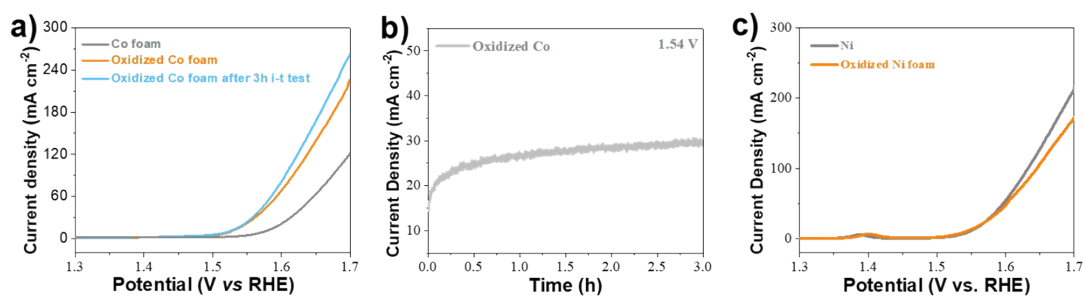


Fig. S14 Electrocatalytic activity of directly oxidized metal foams. The electrochemical oxidation process was conducted with i-t method for 5h at current density of about 20 mA cm^{-2} . a) LSV curve of directly oxidized Co foam. For comparison, LSV curves of pristine Co foam and the oxidized Co foam that was experienced for another 3h of i-t test (shown in Fig. S14b). b) I-t curve of electrochemical oxidized Co foam for another 3h with potential of 1.54 V (vs RHE). c) LSV curve of directly oxidized Ni foam.

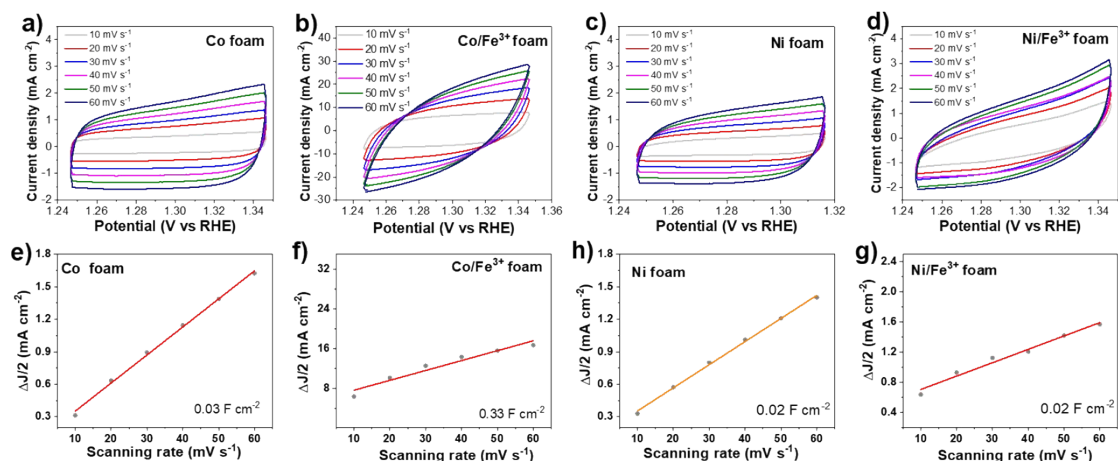


Fig. S15 CV curves of the catalytic electrodes at various scan rates to investigate the specific capacitor values (C_{dl}) that was used to estimate the electrochemical active specific surface area. a, e) Co foam, b, f) Co/Fe³⁺ foam, c, h) Ni foam, d, g) Ni/Fe³⁺ foam.

The higher C_{dl} values indicates the higher electrochemical active specific surface area. The four products present C_{dl} values of 0.03, 0.33, 0.02, 0.02 for Co foam, Co/Fe³⁺, Ni foam, and Ni/Fe³⁺ respectively. However, it should be noted that the thus estimated C_{dl} values are highly influenced by the disturb of Faradic current. In our cases, the C_{dl} values is also highly influenced by variations in the defects in the etched surfaces, micro-/nanotexture in the surfaces of the foams, as well as changes in the resistance of these materials with variations in the oxide layers.

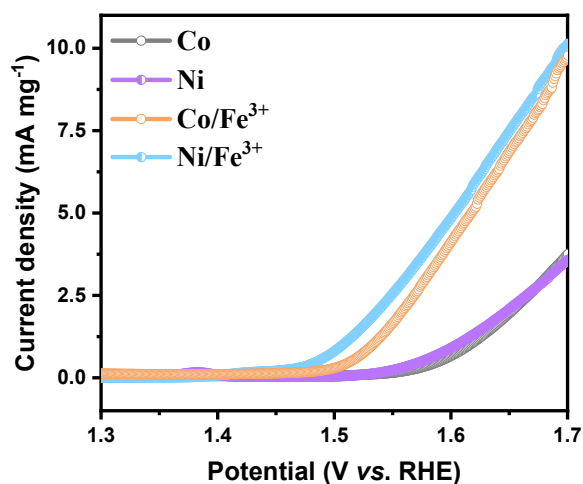


Fig. S16 LSV curves of the catalytic electrodes normalized by foam mass.

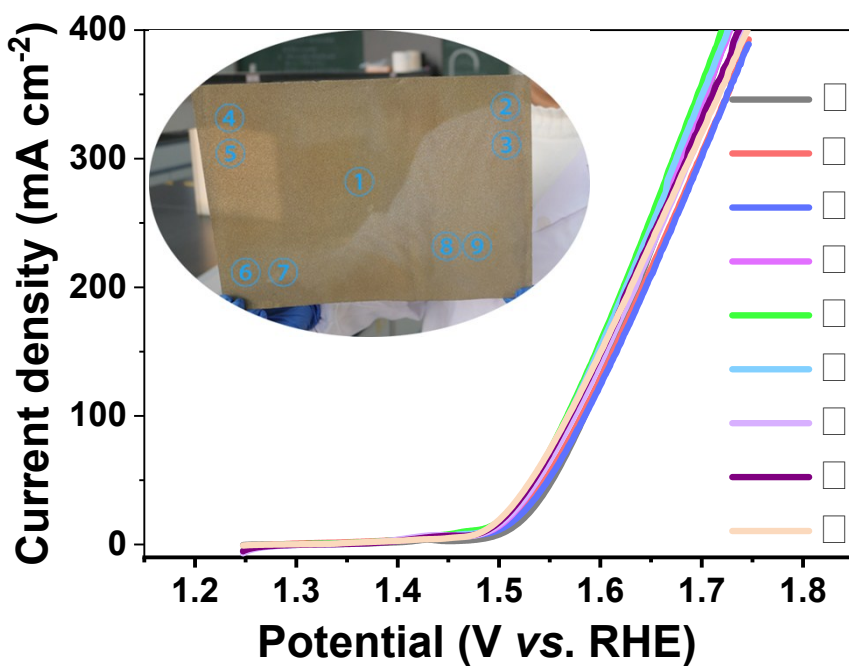


Fig. S17 LSV curves for the randomly taken nine pieces from scale-up prepared Ni/Fe³⁺ foam. Nine different small pieces ($\sim 0.5 \times 1 \text{ cm}^2$) were cut by scissors from the scale-up prepared Ni/Fe³⁺ foam and were then tested towards oxygen evolution with the same method as that shown in the experimental section.

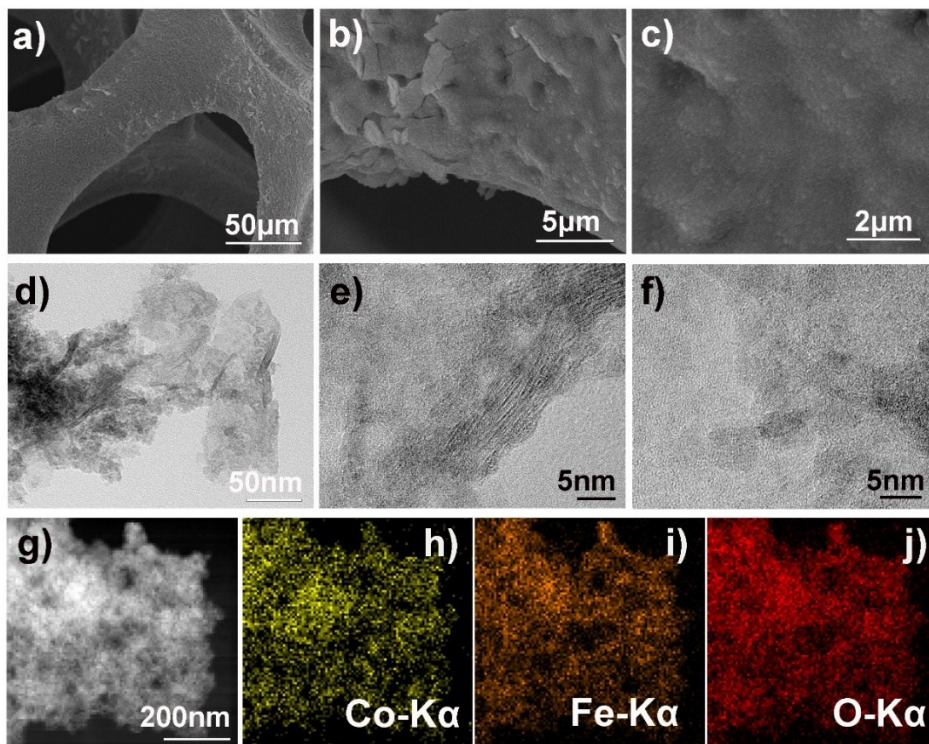


Fig. S18 The characterization results of the Co/Fe³⁺ product after 70 h of OER operation. a-c) SEM images; d-f) TEM and HRTEM images; g-j) Element mapping analysis and the Co, Fe and O distribution.

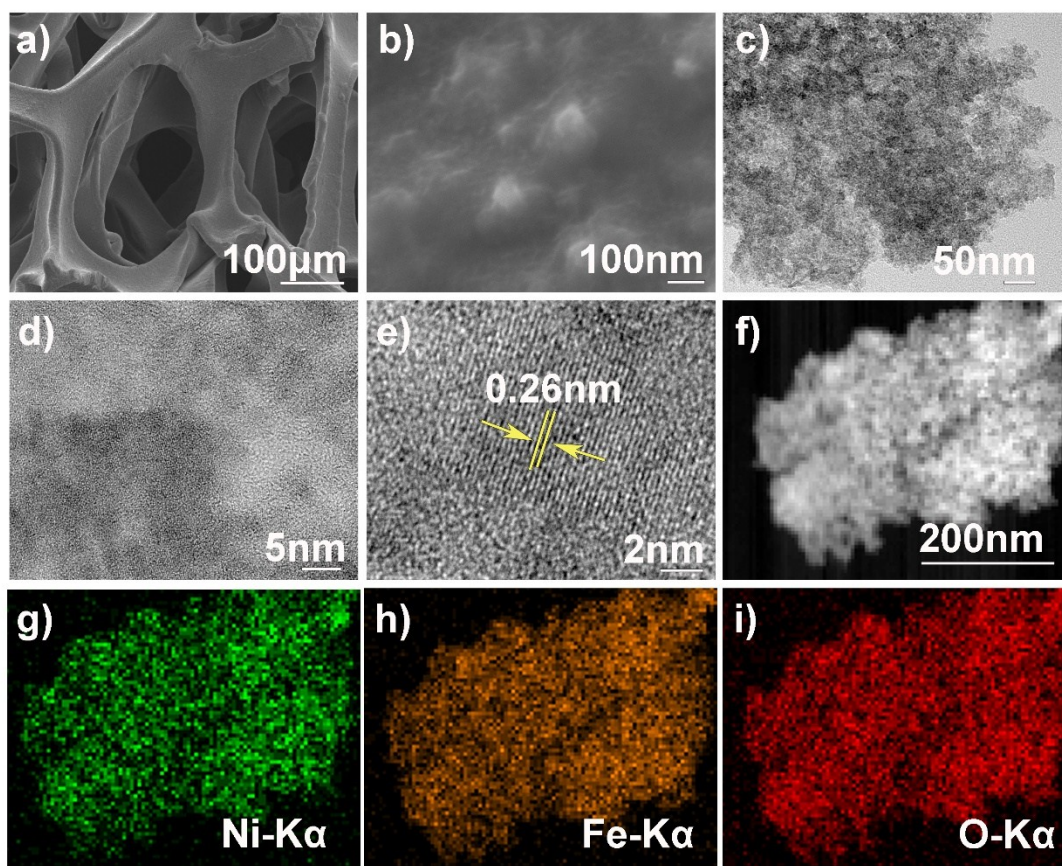


Fig. S19 The characterization results of the Ni/Fe³⁺ product after 70 h of OER operation. a, b) SEM images; c-e) TEM and HRTEM images; f-i) Element mapping analysis and the Ni, Fe, and O distribution. These SEM, TEM, and element mapping analysis results indicate that the microstructure and composition of Ni/Fe³⁺ product after longer time OER operation are basically consistent with the original sample. The lattice spacing observed in d) is 0.26 nm that can be indexed into (012) plane of layered bimetal hydroxides.

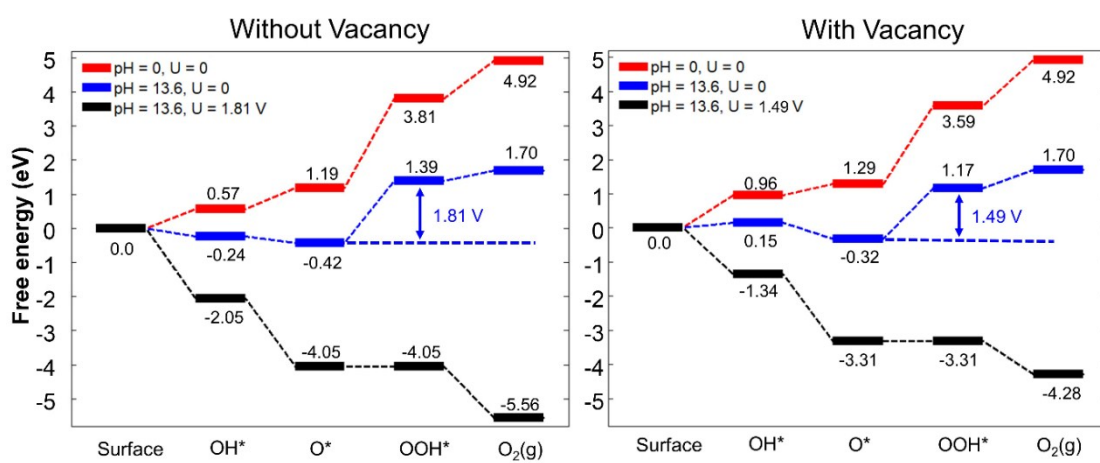


Fig. S20 Calculated free energy profile without (b) and with (c) oxygen vacancy at zero potential and standard condition (red line); at zero potential and basic condition (blue line); at the theoretical overpotential and basic condition (black line).

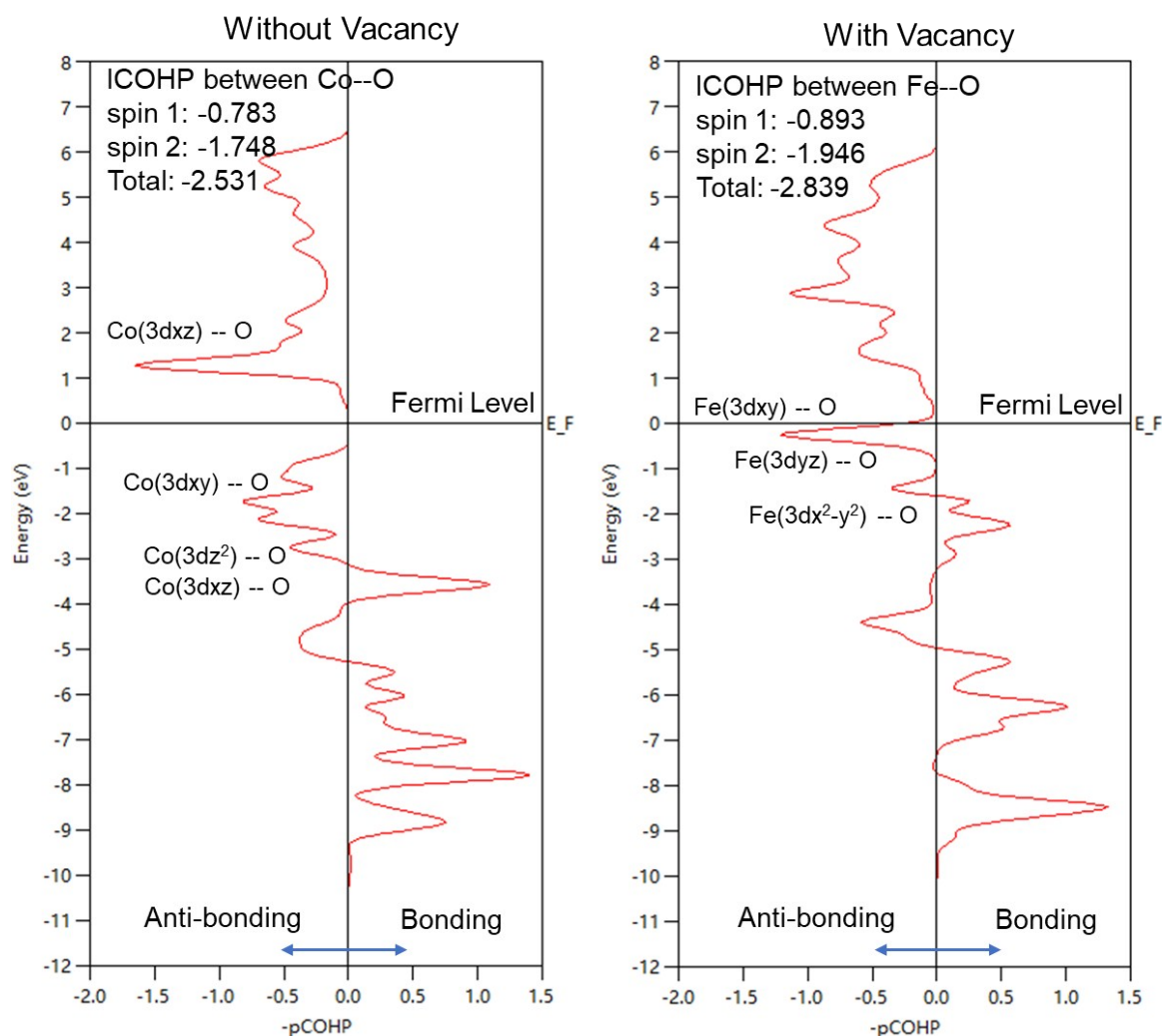


Fig. S21 -pCOHP values per cell of Co-O and Fe-O bonds in Co-OOH and Fe-OOH system. All energies are eV and shown relative to the Fermi level E_F .

To further understand why Fe-OOH bond is stronger than Co-OOH bond, Crystal Orbital Hamilton Populations (COHP) analysis was carried out by LOBSTER 3.1.0 program.¹⁶ Essentially, COHP calculated the overlap of electron clouds between two atoms and shows bonding and antibonding contributions to the band-structure energy. The value of ICOHP is the integral of bonding (negative) and anti-bonding part (positive) under Fermi level; the lower the ICOHP value, the stronger the bonding.

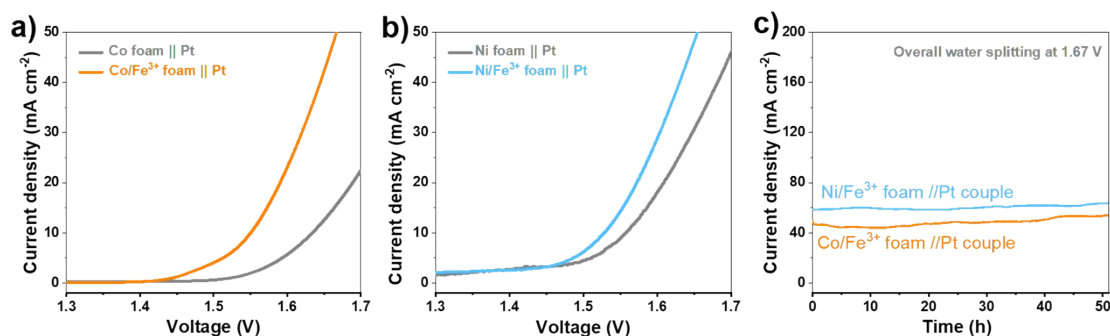


Fig. S22 Overall water splitting of the system composed by a) Co/Fe³⁺ foam//Pt and b) Ni/Fe³⁺ foam//Pt in an alkaline electrolyze. c) Curves of current density versus time obtained over Co/Fe³⁺ foam//Pt and Ni/Fe³⁺ foam//Pt alkaline electrolyze at voltage of 1.67 V.

Details for the overall water splitting test are as follows. Overall water splitting test was conducted with a two electrode system and 1 M KOH aqueous solution as the electrolyte. The prepared metal foam (Co/Fe³⁺ foam and Ni/Fe³⁺ foam) with size of 0.5×1 cm² and a Pt foil (0.5×1 cm²) were used as the anode and cathode, respectively. The scanning rate is 5 mV s⁻¹. For the stability test, a i-t method was used with added potential of 1.67 V.

Table S1. Structural parameters extracted from the Fe K-edge EXAFS fitting ($S_0^2=0.76$).

Sample	Scattering pair	CN	R(Å)	$\sigma^2(10^{-3}\text{Å}^2)$	$\Delta E_0(\text{eV})$	R factor
Co/Fe ³⁺	Fe-O	5.4	2.04	4.7	1.5	0.005
	Fe-O-Co	5.6	3.10	5.9		

S_0^2 is the amplitude reduction factor; CN is the coordination number; R is interatomic distance (the bond length between central atoms and surrounding coordination atoms); σ^2 is Debye-Waller factor (a measure of thermal and static disorder in absorber-scatter distances); ΔE_0 is edge-energy shift (the difference between the zero kinetic energy value of the sample and that of the theoretical model). R factor is used to value the goodness of the fitting. This value was fixed during EXAFS fitting, based on the known structure. Error bounds that characterize the structural parameters obtained by EXAFS spectroscopy were estimated as $N \pm 20\%$; $R \pm 1\%$; $\sigma^2 \pm 20\%$; $\Delta E_0 \pm 20\%$.

Table S2. Comparison studies with the reported catalytic electrodes tested with foam metal or carbon substrates.^a

Materials	Substrates	Synthetic Method	Electrolyte	Overpotential (η , mV) at a current density (mA cm ⁻²)	Tafel slope (mV dec ⁻¹)	Stability	Refs
Co-Fe-P	Ni foam	Solvothermal & calcination	1.0 M KOH	244 (η_{10})	58	for 30 h at 10 mA cm ⁻²	17
FeOOH/Co/FeOOH	Ni foam	Electrodeposition	1.0 M NaOH	250 (η_{20})	32	for 50 h at 20 mA cm ⁻²	18
CoFe ₂ O ₄ /C NRAs	Ni foam	Hydrothermal & calcination	1.0 M KOH	240 (η_{10})	45	for 30 h at 10 mA cm ⁻²	19
FeCo/C NS	Ni foam	Template strategy & ion exchange	1.0 M KOH	219 (η_{10})	74	for 20 h at 10 mA cm ⁻²	20
NiFeB	Ni foam	Chemical-reduction	0.1 M KBi	436 (η_{10})	76	-	21
Ni ₃ S ₂ @MoS ₂ /FeOOH	Ni foam	Hydrothermal & electrodeposition	1.0 M KOH	234 (η_{10})	49	10 mV of η increase after 50 h at 10 mA cm ⁻²	22
Co _{0.75} Ni _{0.25} (OH) ₂	Carbon fiber paper	Laser ablation	1.0 M KOH	235 (η_{10})	56	5% of current loss after 12 h at 10 mA cm ⁻²	23
Cu(OH) ₂ @CoCO ₃ (OH) ₂ ·nH ₂ O	Cu foam	Chemical bath deposition	1.0 M KOH	270 (η_{50})	78	for 20 h at η of 260 mV	24
CoMn(OH) _x -CO ₃ ²⁻	Ni foam	Hydrothermal	1.0 M KOH	294 (η_{30})	-	10 mV of η increase after 18 h at 50 mA cm ⁻²	25
Co(OH) ₂ -TCNQ/ CF	Cu foam	Electrochemical oxidation	1.0 M KOH	276 (η_{25})	101	for 25 h at η of 295 mV	26
Co@MoS ₂	Co foam	ALD	1.0 M KOH	270 (η_{10})	74	34 mV of η increase after 50 h at 100 mA cm ⁻²	27
CoCO ₃ @CoSe	Ni foam	Hydrothermal method	1.0 M KOH	255 (η_{10})	66.4	for 1000 CV cycles	28
Co@Co ₉ S ₈	Co foam	Hydrothermal	1.0 M KOH	350 (η_{10})	55	for 50 h at 20 mA cm ⁻²	29
Co-Pi/graphene	3D graphene	CVD & electrodeposition	0.1 M KP _i	315 (η_{10})	59	for 8 h at 1 V (vs NHE) in 0.1 M KOH	30
CoP nanosheets	Carbon cloth	Hydrothermal & calcination	1.0 M KOH	300 (η_{10})	85	for 10 h at < 20 mA cm ⁻²	31
CoS-Co(OH) ₂ @MoS _{2-x}	Ni foam	Reflux	1.0 M KOH	380 (η_{10})	68	for 28 h at 10 mA cm ⁻²	32
NiS microspheres	Ni foam	Calcination	1.0 M KOH	335 (η_{50})	89	for 20 h at 290 mV (< 20 mA cm ⁻²)	33
Activated 316L stainless steel	Stainless steel	Electrochemical deposition activation	1.0 M KOH	330 (η_{100})	-	for 300 h	34
Ni42 steel	Ni42 steel	Electrooxidation	0.1 M KOH	320 (η_{10})	71.6	for 2000 s at η of 254 mV	35
IrO ₂ -RuO ₂	Ti sheet	PVD sputter	0.1 M KOH	351 (η_{10})	90	-	36
IrO ₂	Glass carbon electrode	Commercial IrO ₂	1 M KOH	520 (η_{10})	66	-	37
NiFe layered double hydroxides	Ti mesh	Hydrothermal method	1.0 M KOH	263 (η_{10})	90	-	38
Co/Fe ³⁺ foam	Co foam	Immersing	1.0 M KOH	262 (η_{10})	62.2	For 70 h at 50 mA cm ⁻²	this work
Ni/Fe ³⁺ foam	Ni foam	Immersing	1.0 M KOH	239 (η_{10})	70.5	for 70 h at 20 mA cm ⁻²	this work

^aBe noted that although we show the substrates, synthetic method, electrolyte for these studies, the current density normalization factors are not equivalent in these studies.

Table S3. Calculated bader charge of OH and OOH adsorption over CoFe-hydroxide surface with and without O vacancy.

	Fe	Co	O	O	H
Without vacancy Co-OH		1.36		-1.05	0.55
Without vacancy Co-OOH		1.41	-0.67	-0.50	0.59
With vacancy Fe-OH	1.35			-1.07	0.55
With vacancy Fe-OOH	1.48		-0.66	-0.56	0.57

References

1. J. P. Perdew, K. Burke and M. Ernzerhof, *Phys. Rev. Lett.*, 1996, **77**, 3865-3868.
2. G. Kresse and J. Furthmüller, *Comput. Mater. Sci.*, 1996, **6**, 15-50.
3. G. Kresse and J. Hafner, *Phys. Rev. B*, 1994, **49**, 14251-14269.
4. G. Kresse and D. Joubert, *Phys. Rev. B*, 1999, **59**, 1758-1775.
5. P. E. Blöchl, O. Jepsen and O. K. Andersen, *Phys. Rev. B*, 1994, **49**, 16223-16233.
6. J. Klimeš, D. R. Bowler and A. Michaelides, *Phys. Rev. B*, 2011, **83**, 195131.
7. J. Zhang, J. Liu, L. Xi, Y. Yu, N. Chen, S. Sun, W. Wang, K. M. Lange and B. Zhang, *J. Am. Chem. Soc.*, 2018, **140**, 3876-3879.
8. M. Bajdich, M. García-Mota, A. Vojvodic, J. K. Nørskov and A. T. Bell, *J. Am. Chem. Soc.*, 2013, **135**, 13521-13530.
9. L. Wen, X. Zhang, J. Liu, X. Li, C. Xing, X. Lyu, W. Cai, W. Wang and Y. Li, *Small*, 2019, **15**, 1902373.
10. W. Tang, E. Sanville and G. Henkelman, *J. Phys. Condens. Matter*, 2009, **21**, 084204.
11. J. Zhang, J. Liu, L. Xi, Y. Yu, N. Chen, S. Sun, W. Wang, K. M. Lange and B. Zhang, *J. Am. Chem. Soc.*, 2018, **140**, 3876-3879.
12. L. Wen, X. Zhang, J. Liu, X. Li, C. Xing, X. Lyu, W. Cai, W. Wang and Y. Li, *Small*, 2019, **15**, 1902373.
13. M. Bajdich, M. Garcia-Mota, A. Vojvodic, J. K. Norskov and A. T. Bell, *J. Am. Chem. Soc.*, 2013, **135**, 13521-13530.
14. Y. Mao, Z. Wang, H.-F. Wang and P. Hu, *ACS Catal.*, 2016, **6**, 7882-7891.
15. Z. Wang, X. M. Cao, J. Zhu and P. Hu, *J. Catal.*, 2014, **311**, 469-480.
16. S. Maintz, V. L. Deringer, A. L. Tchougréeff and R. Dronskowski, *J. Comput. Chem.*, 2016, **37**, 1030-1035.
17. T. Zhang, J. Du, P. Xi and C. Xu, *ACS Appl. Mater. Interf.*, 2017, **9**, 362-370.
18. J.-X. Feng, H. Xu, Y.-T. Dong, S.-H. Ye, Y.-X. Tong and G.-R. Li, *Angew. Chem. Int. Ed.*, 2016, **55**, 3694-3698.

19. X.-F. Lu, L.-F. Gu, J.-W. Wang, J.-X. Wu, P.-Q. Liao and G.-R. Li, *Adv. Mater.*, 2017, **29**, 1604437.
20. R. Xiang, Y. J. Duan, C. Tong, L. S. Peng, J. Wang, S. S. A. Shah, T. Najam, X. Huang and Z. D. Wei, *Electrochim. Acta*, 2019, **302**, 45-55.
21. D. Guo, S. Han, R. Ma, Y. Zhou, Q. Liu, J. Wang and Y. Zhu, *Micropor. Mesopor. Mat.*, 2018, **270**, 1-9.
22. M. Zheng, K. Guo, W.-J. Jiang, T. Tang, X. Wang, P. Zhou, J. Du, Y. Zhao, C. Xu and J.-S. Hu, *Appl. Catal. B-Environm.*, 2019, **244**, 1004-1012.
23. X. Wang, Z. Li, D. Y. Wu, G. R. Shen, C. Q. Zou, Y. Feng, H. Liu, C. K. Dong and X. W. Du, *Small*, 2019, **15**, 9.
24. L. Xie, C. Tang, K. Wang, G. Du, A. M. Asiri and X. Sun, *Small*, 2017, **13**, 1700805.
25. T. Tang, W.-J. Jiang, S. Niu, N. Liu, H. Luo, Y.-Y. Chen, S.-F. Jin, F. Gao, L.-J. Wan and J.-S. Hu, *J. Am. Chem. Soc.*, 2017, **139**, 8320-8328.
26. D. Wu, Y. Wei, X. Ren, X. Ji, Y. Liu, X. Guo, Z. Liu, A. M. Asiri, Q. Wei and X. Sun, *Adv. Mater.*, 2018, **30**, 1705366.
27. D. Xiong, Q. Zhang, W. Li, J. Li, X. Fu, M. F. Cerqueira, P. Alpuim and L. Liu, *Nanoscale*, 2017, **9**, 2711-2717.
28. R. H. Que, G. Ji, D. S. Liu, M. L. Li, X. H. Wang and S. P. Jiang, *Energy Technol.*, 2019, **7**, 9.
29. D. Xiong, Q. Zhang, S. M. Thalluri, J. Xu, W. Li, X. Fu and L. Liu, *Chem. Eur. J.*, 2017, **23**, 8749-8755.
30. M. Zeng, H. Wang, C. Zhao, J. Wei, W. Wang and X. Bai, *Science Bulletin*, 2015, **60**, 1426-1433.
31. T. Liu, L. Xie, J. Yang, R. Kong, G. Du, A. M. Asiri, X. Sun and L. Chen, *ChemElectroChem*, 2017, **4**, 1840-1845.
32. T. Yoon and K. S. Kim, *Adv. Funct. Mater.*, 2016, **26**, 7386-7393.
33. W. Zhu, X. Yue, W. Zhang, S. Yu, Y. Zhang, J. Wang and J. Wang, *Chem. Commun.*, 2016, **52**, 1486-1489.
34. F. Moureaux, P. Stevens, G. Toussaint and M. Chatenet, *Appl. Catal. B: Environm.*, 2019, **258**, 117963.
35. H. Schäfer, D. M. Chevrier, P. Zhang, J. Stangl, K. Müller-Buschbaum, J.D. Hardege, K. Kuepper, J. Wollschläger, U. Krupp, S. Dühnen, M. Steinhart, L. Walder, S. Sadaf and M. Schmidt, *Adv. Funct. Mater.*, 2016, **26**, 6402-6417.
36. H. Schäfer, K. Kupper, J. Wollschläger, N. Kashaev, J. Hardege, L. Walder, S. M. Beladi-Mousavi, B. Hartmann-Azanza, M. Steinhart and S. Sadaf, *ChemSusChem*, 2015, **8**, 3099-3110
37. J. Z. Liu, J. W. Nai, T. T. You, P. F. An, J. Zhang, G. S. Ma, X. G. Niu, C. Y. Liang, S. H. Yang and L. Guo, *Small*, 2018, **14**, 1703514.
38. J. F. Zhang, J. Y. Liu, L. F. Xi, Y. F. Yu, N. Chen, S. H. Sun, W. C. Wang, K. M. Lange, B. Zhang, *J. Am. Chem. Soc.*, 2018, **140**, 3876-3879.